Supplementary material

S1: Time series of sand and fine fluxes inferred from index concentration and sediment discharge measurements

The point sampling method allows for accurate assessment of mean sand concentration when a sufficient number of samples are collected and the river cross-section is thoroughly explored using a well-designed grid of sampling points. However, these measurements are typically performed on an episodic basis, primarily due to operational constraints and cost considerations. Furthermore, as demonstrated in this study, there is no straightforward relationship between discharge and sand concentration in the Ucayali floodplain. As a result, only the surface-based monitoring of sand concentration, carried out by field observers under the CZO HyBAm framework, enables the construction of continuous time series of suspended sand fluxes.

At lowland stations, however, concentrations derived from this monitoring approach are subject to substantial uncertainty.

- This is because samples collected at the free surface, where turbulent mixing is significantly reduced, tend to exhibit low sand mass fractions. Although it is theoretically possible to determine a site-specific ratio α_s between these surface concentrations and the depth-averaged mean sand concentration using the model of Santini et al. (2019), the associated uncertainty remains high. This is particularly true for the range of Rouse numbers observed at the study sites (0.3 < P_s < 0.5), as also discussed by Santini et al. (2019).
- In this study, we aim to reconcile the available data by combining the time series of cross-sectionally averaged total suspended sediment concentration, $C = \alpha C_{\chi}$ (mg l⁻¹) derived from surface index concentration monitoring $C_{\chi}(z \cong h)$ (mg l⁻¹), with the cross-sectional concentrations obtained from *in situ* point sampling. A time series of cross-sectionally averaged sand concentration C_s is derived from the monitored index concentration using an empirical relationship between C and C_s calibrated from gauging data (Fig. S1). The α ratios used were those computed by Santini et al. (2019).
- It is important to note that the empirical relationship between total suspended sediment and sand concentrations was observed in only a few rivers of the Amazon Basin, and therefore cannot be generalized. This limitation highlights the need to explicitly model sand transport dynamics rather than rely solely on empirical extrapolation.

The fine sediment fluxes are calculated following the same method (Fig. S1).

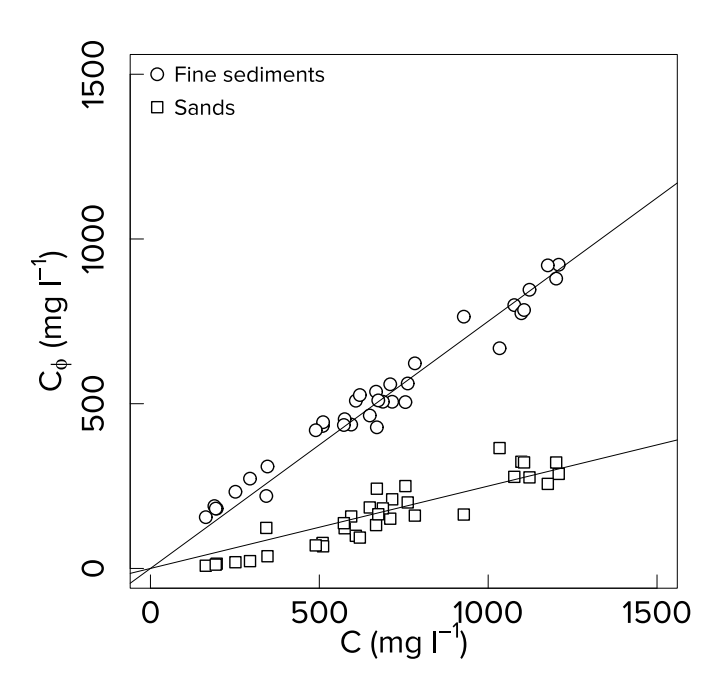


Figure S1: Empirical relationships at Requena between the total cross-sectionally averaged suspended sediment concentration C, and the corresponding cross-sectional concentrations C_{ϕ} of each sediment fraction, where $\phi = f$ denotes fine sediments $\phi = s$ denotes sands.

S2: Triangular floodplain cross-section

When the floodplain cross-section is assumed to be triangular, the water height *h* in the main channel can be obtained by solving the following second-order polynomial equation (the physically meaningful solution is the greater of the two roots), derived from basic geometric considerations:

$$\left(\frac{\Delta x_i}{2\tan(\theta_{fp,i})}\right)(h_i^t)^2 + \Delta x_i \left(B_i - \frac{h_{f,i}}{\tan(\theta_{fp,i})}\right)h_i^t + \Delta x_i \frac{h_{f,i}^2}{\tan(\theta_{fp,i})} = V_i^t,$$
(S2.1)

where θ_{fp} (rad) is a calibrated angle representing the riverward slope of the floodplain, which determines the floodplain width W_{fp} .

40 S3: Additional flow resistances: impact on the velocity and transport capacity when the floodplain is active

In a 2d context, the transverse profiles of θ' and C_b^* could be more affected than the lateral profile of depth-averaged velocity. The velocity declines induced by the floodplain drag, at least near the banks and on the bars, should lead to the sedimentation of finer materials (such as very fine sands, silts, and even clay aggregates) compared to a scenario without this additional flow resistance. According to the Yalin-Shields curve, this would result in an increase in the critical shear stress, which in turn reduces the bottom reference concentration C_b^* (Eq. 12). Furthermore, the Darcy-Weisbach factor could also decrease, leading

to a reduction of θ' . The geometry of bedforms could also be impacted. Thus, the repartition of total shear stress θ between grain-related θ' and bedform-related θ'' dimensionless shear stresses could also change. Indeed, according to the momentum concept, $\theta = \theta' + \theta''$, any increase or decrease in θ'' would impact θ' , then C_b^* and consequently the transport capacity Q_s^* . Among the poorly understood other possible effects, the large and mesoscale secondary currents induced by the floodplain activation could weaken the turbulent velocity profiles in the upper part of the flow (e.g. Guo and Julien, 2008), resulting in a decline in velocities above a dipping point. This would lead to a reduction in the diffusivity ratio β , and thus an attenuation of the sand suspension (hence of Q_s^*) in this flow region.

To account for these complex effects on transport capacity Q_s^* , another shape factor γ (–) has been introduced to adjust the transport capacity Q_{scf0}^* which was initially calculated using the corrections for θ' and u_* corrections in Eqs. 29 and 30.

55
$$Q_{s_{cf}}^* = \gamma \ Q_{s_{cf0}}^*$$
 (S3.1)

In a 2d context, ζ_n can be also interpreted as a shape coefficient between the depth integrated velocity profiles $\overline{u_c}(y)$ and $\overline{u_{cf}}(y)$ in the transverse direction y:

$$\zeta_n = \frac{\frac{1}{B} \int_0^B \overline{u_{cf}(y)} \, dy}{\frac{1}{B} \int_0^B \overline{u_{c}(y)} \, dy},$$
 (S3.2)

and the shape correction factor γ relates to the following ratio:

$$60 \quad \gamma = \frac{\frac{1}{B} \int_0^B Q_{Scf}^*(y) \, dy}{\frac{1}{B} \int_0^B Q_{Scf0}^*(y) \, dy}.$$
 (S3.3)

Here, it was assumed that γ should be a function of ζ_n :

$$\gamma = \lambda \zeta_n^{\xi} \,, \tag{S3.4}$$

with $\lambda \leq 1$ a coefficient and ξ (–) an exponent to calibrate. As ζ_n is between 0 and 1, λ is not useful and this parameter was thus eliminated in order to simplify the model calibration. Thus, when the floodplain is active (*i.e.* when $h > h_f$), the attenuation of the transport capacity is calculated as following:

$$Q_{s_{cf_{i}}}^{*t} = \zeta_{n_{i}}^{\eta t} Q_{s_{cf0_{i}}}^{*t}, \tag{S3.5}$$

where the exponent η includes the term λ .

70

S4: Additional flow resistances: typical example of bed roughness influence in the Amazonian Basin

The Chazuta gauging station (-6.5704°, -76.1193°) on the Huallaga River (a tributary of the Marañón River), also monitored by the CZO HyBam, is a typical example of the influence of bed roughness on flow resistance, as well as an illustration of the increased flow resistance when the floodplain becomes active (Fig. S4).

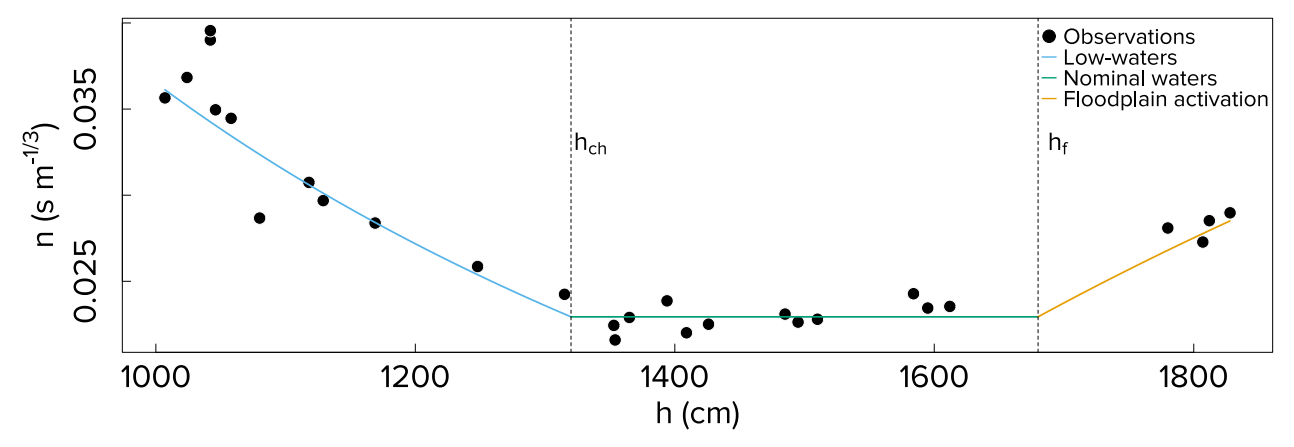


Figure S4: Typical evolution of the Manning coefficient with water level at the Chazuta station on the Huallaga River. Black dots indicate Manning values derived from ADCP gaugings, the blue line shows Manning modelled according to Eq. 32, and the orange line shows Manning modelled according to Eq. 28. Dashed vertical lines represent the water levels h_{ch} and h_f .

85

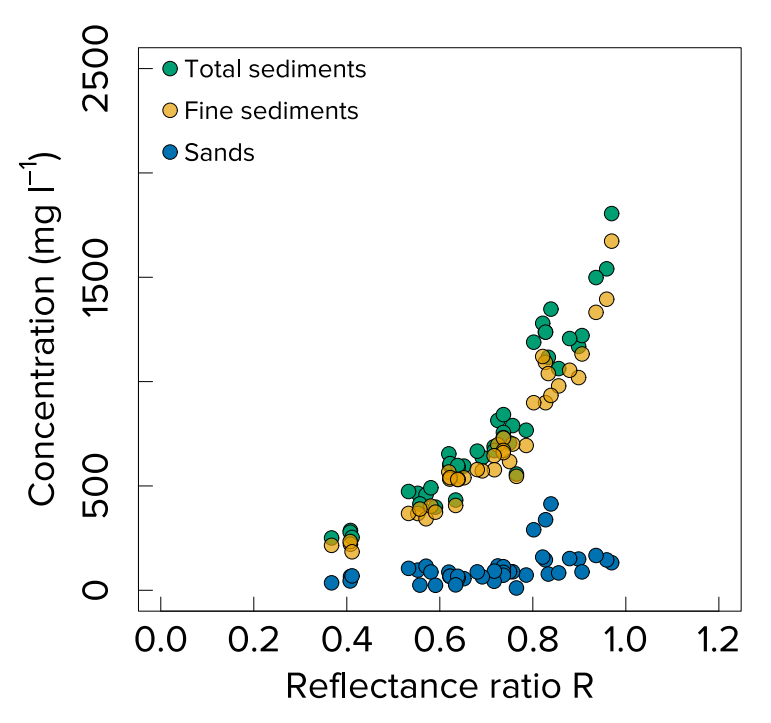
90

95

S5: Negligible optical contribution of sand to surface reflectance

110

100 No significant relationship was found between surface sand concentration and the reflectance ratio measured during field campaigns (Fig. S5). This confirms that the backscattering contribution of sand particles is negligible compared to that of fine sediments, as predicted by Mie theory (Pinet, 2017). Furthermore, the relationship between reflectance ratio and sediment concentration improves when sand is excluded from the concentration estimates.



105 **Figure S5:** Concentrations of total suspended sediments (green dots), fine sediments (orange dots) and sand fractions (blue dots) at the water surface plotted against the reflectance ratio (NIR/Red) measured during calibration—validation campaigns using hyperspectral radiometers.